Direct Numerical Simulations to Investigate Energy Transfer between Meso- and Synoptic Scales

MASIH EGHDAMI

Pratt School of Engineering, Duke University, Durham, North Carolina

SHANTI BHUSHAN

Department of Mechanical Engineering, Mississippi State University, Mississippi State, Mississippi

ANA P. BARROS

Pratt School of Engineering, Duke University, Durham, North Carolina

(Manuscript received 26 July 2017, in final form 18 December 2017)

ABSTRACT

Understanding the development of the atmospheric energy spectrum across scales is necessary to elucidate atmospheric predictability. In this manuscript, the authors investigate energy transfer between the synoptic scale and the mesoscale using direct numerical simulations (DNSs) of two-dimensional (2D) turbulence transfer under forcing applied at different scales. First, DNS results forced by a single kinetic energy source at large scales show that the energy spectra slopes of the direct enstrophy cascade are steeper than the theoretically predicted −3 slope. Second, the presence of two inertial ranges in 2D turbulence at intermediate scales is investigated by introducing a second energy source in the meso-α-scale range. The energy spectra for the DNS with two kinetic energy sources exhibit flatter slopes that are closer to −3, consistent with the observed kinetic energy spectra of horizontal winds in the atmosphere at synoptic scales. Further, the results are independent of model resolution and scale separation between the two energy sources, with a robust transition region between the lower synoptic and the upper meso-α scales in agreement with classical observations in the upper troposphere. These results suggest the existence of a mesoscale feedback on synoptic-scale predictability that emerges from the concurrence of the direct (downscale) enstrophy transfer in the synoptic scales and the inverse (upscale) kinetic energy transfer from the mesoscale to the synoptic scale in the troposphere.

1. Introduction

Atmospheric flows at synoptic scales are often assumed to show a two-dimensional (2D) behavior because of the fact that horizontal scales are considerably larger than the vertical scales (Charney 1971), besides limitations of the analogy between 2D turbulence and quasigeostrophic turbulence in Earth's rotating atmosphere (Tung and Orlando 2003a,b). Reducing the flow dimensions from three to two (horizontal) requires conservation of the total enstrophy of the flow, a constraint that was first introduced for predicting the behavior of 2D turbulence by Kraichnan (1967). The theoretical kinetic energy (KE) spectrum of a 2D flow regime displays two inertial ranges: an inverse energy flux associated with a −5/3 slope and a direct enstrophy cascade associated with a −3 slope with a logarithmic correction to account for nonlocal transfers (Kraichnan 1971).

The behavior of 2D turbulence in the inertial range has been studied extensively using numerical and experimental models (e.g., Boffetta and Ecke 2012). In particular, scaling analysis of numerical simulations of 2D turbulence in the inertial range using a single energy source (e.g., forcing) fixed at a specific scale showed that turbulent transfer mechanisms depend strongly on the spectral separation between the scales of the energy source, the scale of friction at large scales, and the viscous dissipation scale (Boffetta and Musacchio 2010). A three-dimensional (3D) context is necessary for a realistic approximation of the atmospheric 2D flow independent of the direction of energy transfer. Prior studies of nonrotating stratified turbulence support the

Corresponding author: Ana P. Barros, barros@duke.edu

DOI: 10.1175/JAS-D-17-0216.1

hypothesis that mesoscale turbulence transfers result from a forward anisotropic 3D energy cascade (Lindborg 2006). Rotation does not influence the forward cascade significantly if it is weak (Lindborg 2005), but in the case of strong rotation, energy piles up at the larger scales, a behavior linked to the transition to 2D turbulence (Biferale et al. 2012; Marino et al. 2013). Thus, the two inertial-scale ranges are connected and may interact (Fig. 1), and a strict separation between synoptic and mesoscales would be an unphysical constraint. A universally accepted comprehensive explanation of the physics underlying the horizontal spectrum of atmospheric KE and in particular the observed scaling behavior is still lacking.

The horizontal KE spectra of the atmosphere estimated using aircraft measurements and global radiosonde data from different field experiments (Nastrom and Gage 1985; Cho et al. 1999; Frehlich and Sharman 2010) exhibit a -3 slope in the synoptic range of scales (800–2000 km) and a $-5/3$ slope in the mesoscales (2–600 km). The ability to reproduce this scaling behavior is a key requirement in the evaluation of weather and climate models (e.g., Skamarock 2004; Hamilton et al. 2008; Evans et al. 2013; Skamarock et al. 2014; Nogueira and Barros 2014). The synoptic-scale flow approaches 2D behavior at large scales, and thus, the -3 slope of the observed KE spectra is consistent with the direct enstrophy cascade in the inertial range of 2D turbulence (Cho and Lindborg 2001; Tung and Orlando 2003a; Vallgren et al. 2011).

There is, however, some disagreement in the literature (e.g., Xia et al. 2011; Vallgren et al. 2011; Waite and Snyder 2009) over the direction of net energy transfer in the mesoscales where the slope of the observed spectra is $-5/3$. Waite and Snyder (2009) showed that model simulations of dry mesoscale dynamics in the absence of topography produce $-5/3$ spectra associated with a net forward energy cascade. However, this result does not rule out the coexistence of an inverse energy flux produced by moist convection as in realistic numerical weather simulations (Nogueira and Barros 2014; Sun et al. 2017). The hypothesis, first proposed by Lilly (1989), that a source of energy in the mesoscales is required to develop and maintain the inverse energy transfer flux was explored by Cencini et al. (2011) using a single direct numerical simulation (DNS) of 2D turbulence with modified viscosity (hyperviscosity) and two energy sources with a large-scale gap (wavenumber ratio of 7/240). Whereas the specific range of scales, the scale gap, and the transition scale range of the spectrum in Cencini et al. (2011) are different from the observed atmospheric spectra, they showed that an inertial range developed between the two energy sources with coexisting and overlapping direct enstrophy and inverse energy fluxes dominating the KE budget in vicinity of the energy sources at the large (-3 spectral slope) and small scales ($-5/3$ spectral slope), respectively.

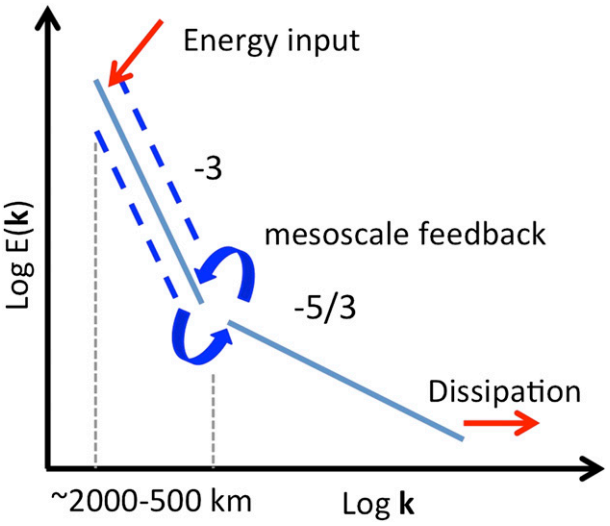

FIG. 1. Conceptual representation of the observed (Nastrom and Gage 1985) scaling behavior in the KE of atmosphere horizontal wind including interactions among synoptic and mesoscales modeled by the second energy feedback here.

The objective of this study is to investigate the behavior of energy transfer in 2D turbulence between the meso-α (~200–600 km) and synoptic (~1000–4000 km) scales toward elucidating the dependence of energy transfer mechanisms on the spectral separation of the two energy sources vis-à-vis the observed scaling behavior in the atmosphere (e.g., Nastrom and Gage 1985). First, the impact of the relative scale of forcing (e.g., location of a single energy source; DNS series S in Table 1) on turbulence transfer is demonstrated. Second, the hypothesis that mesoscale inverse energy transfer significantly impacts enstrophy transfer in the synoptic range is tested using simulations with two energy inputs (DNS series D in Table 2) and for different model resolutions (DNS series H in Table 3). Finally, the adaptive behavior of the enstrophy and inverse energy cascades in the inertial range to scale separation between the two energy inputs is examined (DNS series G in Table 4).

2. DNS experiments

The numerical experiments are based on DNSs of the incompressible Navier–Stokes equations:

$$\frac{\partial u_j}{\partial x_j} = 0, \tag{1a}$$

TABLE 1. Summary of single-energy-source (S) simulation series with $\nu = 10^{-5}$ and grid size $N_c^2 = 2048^2$. The forcing width ($\Delta_f^1 = 1$) is constant for all simulations, and constant nominal energy input rate ϵ_N^1 is reduced to keep the effective energy input ϵ_I^1 constant. Overall, the results show a decreasing trend in the spectral slope due to shifting the energy source from large scales to small scales in the S series. No slope is calculated when the associated inertial range is small.

			Spectral slope	
ID	k_f^1	ϵ_N^1	$k < k_f^{1a}$	$k > k_f^{1b}$
S1	10	8×10^{-5}	—	−3.8
S2	20	4×10^{-5}	−1.5	−3.8
S3	40	2×10^{-5}	−1.8	−4.2
S4	80	1×10^{-5}	−1.7	−4.7
S5	160	5×10^{-6}	−1.6	−4.6
S6	320	2.5×10^{-6}	−1.3	—

[a] Slopes for S series are calculated between wavenumbers ($k_f^1/2$) and ($k_f^1 - \Delta_f^1/2$).

[b] Slopes for S series are calculated between wavenumbers ($k_f^1 + \Delta_f^1/2$) and 256.

$$\frac{\partial u_j}{\partial t} + \frac{\partial (u_l u_j)}{\partial x_l} = -\frac{\partial p}{\partial x_j} + \nu \frac{\partial^2 u_j}{\partial x_l \partial x_l} + \sum_{n=1}^{2} F_j^n, \qquad (1b)$$

where u is the velocity field, x is the space variable, t is time, ν is kinematic viscosity, F_j^n is the forcing term, l and j are tensor indices assuming values of 1 and 2 for 2D flow, and finally, the superscript n differentiates the large- and small-scale forcing terms taking values of 1 and 2, respectively. The equations are solved in nondimensional form, and a detailed description of the solver can be found in Bhushan and Warsi (2007). Specifically, the DNSs are conducted using a pseudospectral solver with a 3/2 dealiasing rule in Fourier space on a double periodic domain $[x_j | x_j \in (-L_j, L_j)$, where $L_j = \pi]$ using a grid defined by N_c^2 collocation points. The numerical scheme consists of three steps. First, a second-order Adams–Bashforth scheme is implemented to solve the convective terms with δt time interval. Next, the pressure correction is applied to the velocity field. The third step incorporates the dissipation terms. Defining the Fourier transform of the velocity field as $u(x, t) = \sum_k e^{ikx} \hat{u}(x, t)$, where k is the wavenumber and the caret indicates the Fourier component, Eqs. (1a) and (1b) reduce to

$$\left(\frac{d}{dt} + \nu k_l k_l\right) \hat{u}_j(k) = -\left(\delta_{jm} - \frac{k_j k_m}{k^2}\right) \{ik_l \hat{u}_m * \hat{u}_l\}(k) + \sum_{n=1}^{2} \hat{F}_j^n, \qquad (2)$$

where $m = 1, 2$ is an index variable, the asterisk represents convolution over all wavenumbers, and δ_{jm} is the Kronecker delta (Pope 2000). The forcing term is defined as

$$\hat{F}_j^n(k) = \begin{cases} \epsilon_N^n \dfrac{\hat{u}_j(k)}{|\hat{u}|^2(k)} & ||k| - k_f^n| < \Delta_f^n/2 \\ 0 & ||k| - k_f^n| \geq \Delta_f^n/2 \end{cases}, \qquad (3)$$

where ϵ_N^n is a constant nominal energy input rate; k_f^n and Δ_f^n are, respectively, the forcing wavenumber and the radial width of the source in wavenumber space; and $|\hat{u}|^2$ is the velocity magnitude. Equation (3) defines the energy input (forcing) and the range of wavenumbers over which it acts in Eq. (2). Thus, the effective energy input is $\epsilon_I^n = \pi \epsilon_N^n k_f^n \Delta_f^n$. As the square of the wavenumber appears in the dissipation term in Eq. (2), the effective dissipation is a function of both kinematic viscosity and the number of collocation points N_c used in the numerical simulation. Following a simple heuristic analysis (Kraichnan 1967; Borue 1993; Eyink 1996; Boffetta and Musacchio 2010), the inverse energy flux and enstrophy cascade directions can be qualitatively determined from

$$\frac{\epsilon_s}{\epsilon_L} = \left(\frac{l_s}{l_f}\right)^2 \left(\frac{l_f}{l_L}\right)^2 \frac{(l_L/l_f)^2 - 1}{1 - (l_s/l_f)^2}, \qquad (4a)$$

TABLE 2. Summary of dual-energy-source (D) simulation series with $\nu = 10^{-5}$ and grid size $N_c^2 = 2048^2$. Nominal energy input rate ($R_N = \epsilon_N^1/\epsilon_N^2$) is increased to increase the effective energy input ($R_I = \epsilon_I^1/\epsilon_I^2$). The forcing width is $\Delta_f^1 = 1$ and $\Delta_f^2 = 2$. Overall, the results show a decreasing trend (steepening) in the spectral slope due to the decrease of the energy intensity of the second source. Slopes for the D series are calculated for wavenumbers 22–60 and 81–256 for intermediate- and small-scale ranges, respectively.

				Spectral slope	
ID	k_f^1/k_f^2	$R_N = \epsilon_N^1/\epsilon_N^2$	$R_I = \epsilon_I^1/\epsilon_I^2$	$k_f^1 < k < k_f^2$	$k > k_f^2$
D1	20/80	$4 \times 10^{-5}/1.0 \times 10^{-5}$	1/2	−1.4	−4.2
D2	20/80	$4 \times 10^{-5}/5.0 \times 10^{-6}$	1	−1.7	−4.2
D3	20/80	$4 \times 10^{-5}/2.5 \times 10^{-6}$	2	−1.9	−4.4
D4	20/80	$4 \times 10^{-5}/1.25 \times 10^{-6}$	4	−2.5	−4.5
D5	20/80	$4 \times 10^{-5}/0.63 \times 10^{-6}$	8	−3.0	−4.5
D6	20/80	$4 \times 10^{-5}/0.31 \times 10^{-6}$	16	−3.5	−4.3

TABLE 3. Summary of simulation series H similar to S2 in all respects, but with higher number of grid collocation points N_c and lower viscosity ν.

ID	Grid (N_c^2)	ν
H1	4096^2	1×10^{-5}
H2	4096^2	4×10^{-6}
H3	7680^2	4×10^{-6}
H4	7680^2	2×10^{-6}

$$\frac{\eta_s}{\eta_L} = \frac{(l_L/l_f)^2 - 1}{1 - (l_s/l_f)^2}, \tag{4b}$$

where ϵ_s and η_s are, respectively, the energy and enstrophy transfer rates to small scales; likewise, ϵ_L and η_L are the energy and enstrophy transfer rates to the larger scales; $l_s^2 = \epsilon_s/\eta_s$ and $l_L^2 = \epsilon_L/\eta_L$ represent, respectively, the characteristic smallest and the largest scale of the system; and finally, l_f is the forcing scale. In a dissipative system, l_s and l_L can be associated with small- and large-scale dissipation characteristic lengths, respectively, (l_ν and l_α) as in Boffetta and Musacchio (2010). Although it is not possible to determine exactly how l_s and l_L are dependent on model physical parameters (such as viscosity), the dominant direction of cascades can be qualitatively deduced in the limits of the equations. The length-scale ratio l_s/l_L is constant if ν and N_c are fixed; however, l_L/l_f and l_s/l_f increase as the forcing scale changes from the larger to the smaller scales. That is, first, ϵ_s/ϵ_L is very small and energy accumulates at the larger scales, and then η_L/η_s is very small and all enstrophy goes to the dissipation range.

A total of 21 DNSs were conducted to test single- versus dual-energy-source behavior and scale separation as a function of effective energy input and grid resolution (viscosity). The specific DNS configurations and the scaling analysis results for each case are presented in Tables 1–4. In the S series (Table 1), the energy input location shifts from the larger scales ($k_f^1 = 10$) to smaller scales ($k_f^1 = 320$) and the effective energy input is constant. In the D series (Table 2), the large-scale energy input is fixed at $k_f^1 = 20$ with the secondary energy source at $k_f^2 = 80$, and the effective energy input ratio ($R_I = \epsilon_I^1/\epsilon_I^2$) decreases as the second energy source is reduced from D1 through D6 by reducing the nominal energy input ratio ($R_N = \epsilon_N^1/\epsilon_N^2$). Four simulations referred to as the H series, in all respects similar to S2 but with increased grid resolution and lower viscosity, were conducted to assess the sensitivity of the DNSs to grid resolution and viscosity as summarized in Table 3. A final set of five simulations, the G series in Table 4, was conducted to examine the sensitivity of the KE spectrum scaling behavior in the inertial range to changes in the scale separation.

TABLE 4. Summary of dual-energy-source (G) simulation series with different scale separations. The forcing width is $\Delta_f^1 = 1$ and $\Delta_f^2 = 2$. DNSs D4 and D6 are included for easy reference.

ID	k_f^1/k_f^2	$R_I = \epsilon_I^1/\epsilon_I^2$	Grid (N_c^2)	ν
D4	20/80	4	2048^2	1×10^{-5}
D6	20/80	16	2048^2	1×10^{-5}
G1	20/160	4	7680^2	4×10^{-6}
G2	20/160	16	7680^2	4×10^{-6}
G3	20/320	2	7680^2	4×10^{-6}
G4	20/320	8	7680^2	4×10^{-6}
G5	20/320	32	7680^2	4×10^{-6}

The DNS experiments were designed such that the energy input at synoptic scale (primary energy source) corresponds to a constant turbulence intensity ϵ_I^1 for both the S and D series. The turbulence intensity of the second energy source was reduced for the D series with R_I varying from 1/2 to 16. Note that the specific effective energy inputs for the dual-source DNSs per se are not relevant, just their relative magnitude. For the G series, R_I varied from 2 to 32, and the injections that predict similar energy spectra as D4 and D6 are used for discussions.

In dimensional terms, considering that the domain length scale is $L_0 = 12\,732$ km, the smallest grid spacing when $N_c = 2048$ is 6 km and for $N_c = 7680$ is 1.66 km. The energy injection scales in the *S* series vary from 4000 to 125 km, thus spanning the full range of synoptic and meso-α scales. For the D series, the primary energy injection is in the synoptic range at 2000 km, and the second injection is in the upper mesoscale range at 500 km (see Fig. 1). For the G series, the primary energy injection remains in the synoptic range at 2000 km, but the secondary injection is shifted successively toward the lower meso-α and meso-β scales, respectively, at 250 ($k_f^2 = 160$) and 125 km ($k_f^2 = 320$). The simulation time step is $2 \times 10^{-4}(L_0/U_0)$ for the 2048^2 grid and $1 \times 10^{-4}(L_0/U_0)$ for the 7680^2 grid. Assuming $U_0 = 10\,\mathrm{m\,s^{-1}}$, the temporal resolutions of the simulations are 0.07 and 0.035 h, respectively.

3. DNS results

Snapshots of selected S2 and D5 $\sqrt{\mathrm{KE}}$ fields at the end of the DNSs are shown in Fig. 2. Turbulence develops faster in D5 in the presence of a second energy source at small scales. Turbulence also develops faster for cases with the single energy source placed at the smaller scales for the single-source S series (not shown).

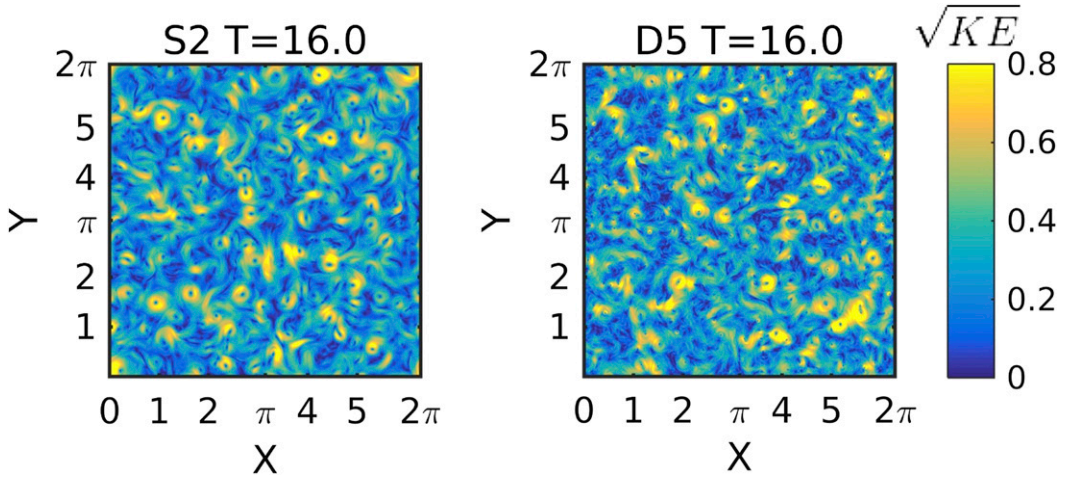

FIG. 2. Instantaneous $\sqrt{\text{KE}}$ fields for (left) S2 and (right) D5 at $T = 16$.

The temporal evolution of S2 spectra is shown in Fig. 3a. Despite the absence of large-scale friction, the spectral slopes do not change with time, suggesting 2D turbulence is well developed after $T = 6$ for the enstrophy cascade inertial range ($k > k_f^1$), which is in agreement with previous results (Vallgren and Lindborg 2011). Energy piles up at large scales ($k < k_f^1$) as expected, but this does not affect the spectra to the right of the energy injection. Evidence of both energy and enstrophy transfer is present in the KE spectra of S simulations at scales larger and smaller than the scale of the forcing, respectively. The spectral slope in the enstrophy cascade region is, however, much steeper than the observed and theoretical values of -3 for all single-energy-source simulations (Table 1), a behavior that is consistent with the literature for similar simulations (e.g., Lindborg and Alvelius 2000; Vallgren and Lindborg 2011). Results from DNSs with resolutions as high as $16\,384^2$ (Boffetta 2007) and later $32\,768^2$ (Boffetta and Musacchio 2010) show that the spectral slope right below the source of energy in the enstrophy cascade range is steeper (about -3.35) than the theoretically predicted value (-3) and might be even steeper in the presence of large-scale drag, as suggested by Vallgren and Lindborg (2011). Nevertheless, the enstrophy cascade always forms for higher wavenumbers to the right of the source of energy and reaches quasi-stationary state.

The spectral slopes for the dual-energy-source DNSs (D series) are flatter than S2 (Fig. 3b; Table 2), gradually steepening from slopes less than $-5/3$ for D1 to values closer to -3 for D5. Overall, the scaling analysis suggests that the energy transfer mechanism in the synoptic scales changes from approaching the behavior of a kinetic energy cascade (e.g., D1) to approaching the behavior of an enstrophy cascade (e.g., D5) as the magnitude of the second energy input decreases relative to the primary source (i.e., as R_I increases). A key implication of these results is that, albeit of smaller magnitude, the second energy source in the upper meso-α-scale range is necessary to develop the enstrophy cascade with a -3 spectral slope in the synoptic scales. That is, the second energy source functions as a feedback mechanism between the meso- and synoptic scales.

Figure 4 shows the temporal evolution of the kinetic energy for the S and D simulations. Again, it is apparent that turbulence develops faster when energy input is in the higher wavenumbers, consistent with the results for all D simulations. The final energy in the inertial range is always higher for the D series compared to S2, as expected; however, in the cases of D1, D2, and D3 ($R_I \leq 2$), more energy is going to the synoptic scales where it lives longer. In the cases of D4, D5, and D6 ($R_I \geq 4$), which show a scaling behavior closer to the observations in the atmosphere (a -3 slope), the energy is about the same as in S2, which exhibits a much steeper spectral slope. The energy transfer in the synoptic scales is therefore modified significantly by the presence of a feedback from the mesoscales as small as 12.5% (e.g., D5) of the magnitude of the synoptic energy source.

The results only depend on the boundary conditions imposed on the system, that is, the intensity and the scale of the forcing F_j^n, and do not exhibit sensitivity to increased grid resolution or the kinematic viscosity. This is illustrated by Fig. 5, which shows the energy spectra for simulations H1, H2, H3, and H4 (Table 3) compared against S2 at simulation time $T = 12$, focusing on the enstrophy inertial range between $k_f^1 = 20$ and $k_f^2 = 80$ as per Fig. 3a. The spectra do not change with time after

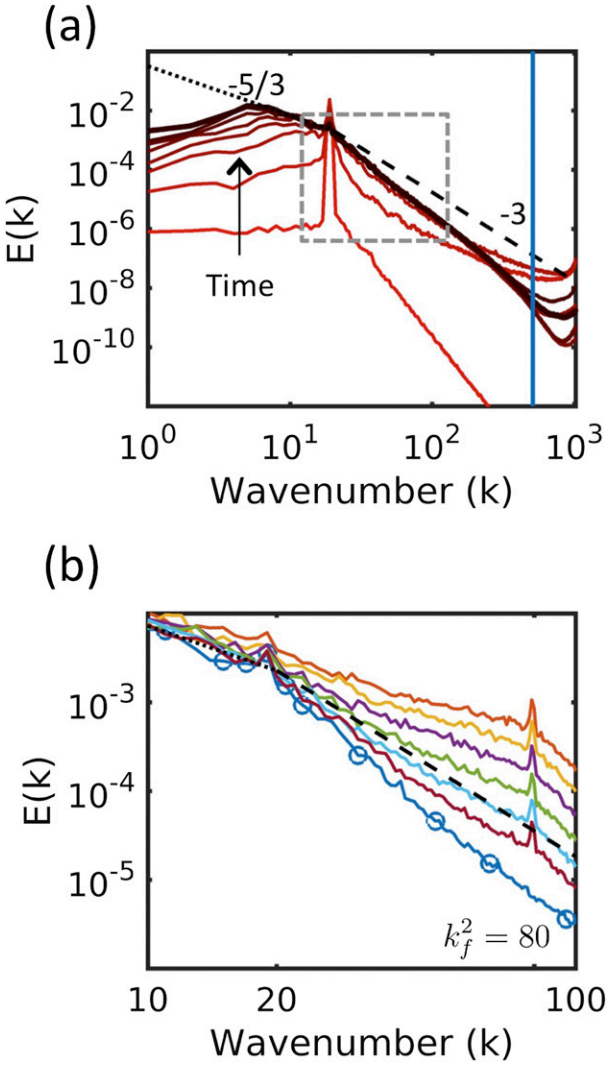

FIG. 3. (a) Time evolution of energy spectra for S2; solid lines from the bottom to top are at simulation times 2, 4, 6, 8, 10, 12, 14, and 16, lines with −5/3 (dotted) and −3 (dashed) slopes are shown for comparison, and a vertical line shows the four times of the smallest wavenumber in the system. The vertical line in marks the Nyquist wavenumber. (b) The inset of region of (a) with the terminal energy spectra of S2 (line with circles) and D series; solid lines from top to bottom are D1, D2, D3, D4, D5, and D6, respectively, and the dashed line with a −3 slope is shown for comparison.

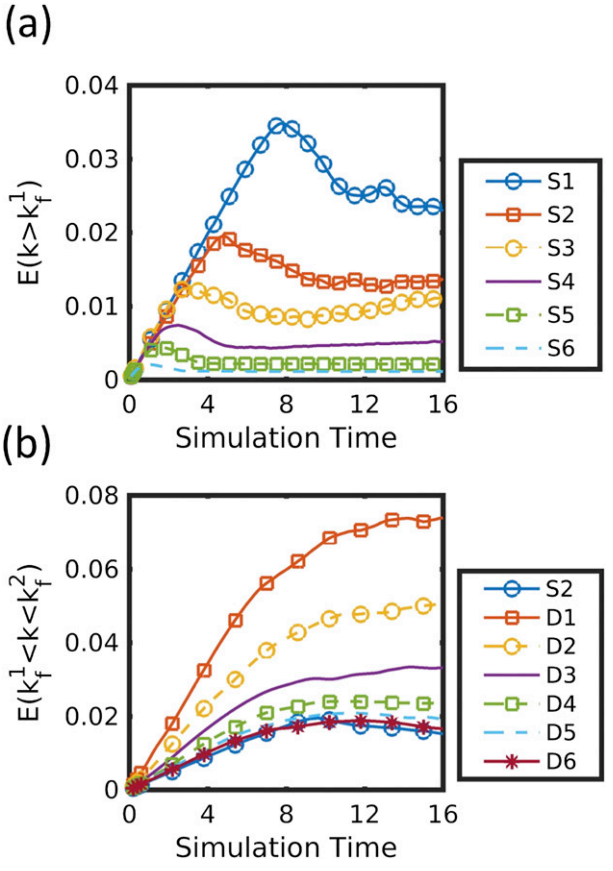

FIG. 4. Time evolution of (a) KE of wavenumbers below the forcing wavenumber k_f^1 for S series and (b) KE of wavenumbers between $k_f^1 = 20$ and $k_f^2 = 80$ for the D series compared with S2.

$T = 8.0$, and all spectra show the same slope of −3.8 as for the S2 case in the synoptic range. Thus, increasing the grid resolution and/or viscosity also does not affect the large scales. This is expected since information travels downscale in the enstrophy cascade, and the small scales outside the inertial range should not influence the large scales in stable numerical experiments.

The enstrophy $\Pi_Z(k)$ and energy $\Pi_E(k)$ transfers attributed to the nonlinear terms in Eq. (1b) are shown in Fig. 6 for series S and D (see also Boffetta and Musacchio 2010; Pope 2000). The localized jumps that are especially evident in the energy transfer plot (bottom panel) correspond to the position of energy inputs. Detailed examination of S2 and S4 in the light of Eqs. (4a) and (4b) provides insight into the energy transfer direction. In the case of S2, with large-scale separation between the forcing and viscous dissipation scales, the energy input is mostly transferred to larger scales rather than cascading down to the smaller scales. The enstrophy cascade for S4 is significantly larger than for S2. For cases with two energy sources, turbulent transfer in the intermediate wavenumber range ($20 < k < 80$) depends on the scale separation between the inputs and on the ratio R_N of the first and second nominal energy sources. If the second energy injection is strong (e.g., D2), the inverse energy cascade dominates between the input wavenumbers as long as $R_I \leq 2$, and the spectral slope for these cases is closer to −5/3, as expected in 2D turbulence left of the injection. If the second energy injection is weak (e.g., D5), the enstrophy cascade due to

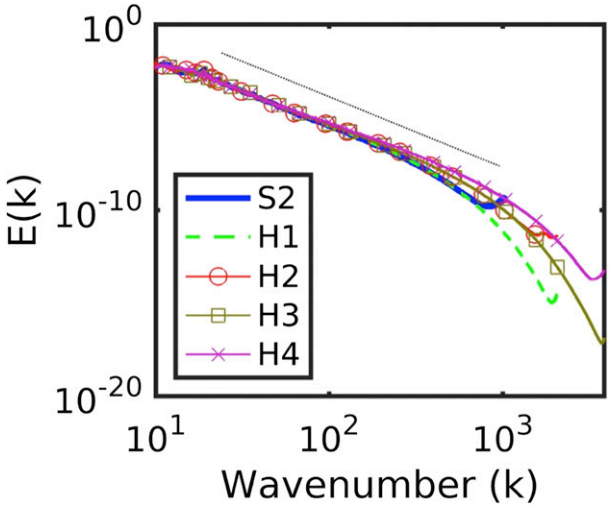

FIG. 5. Energy spectra of S2 and H series for $T = 12.0$. The black dotted line with a -3.8 slope (parallel to S2; see Table 1) is provided for reference.

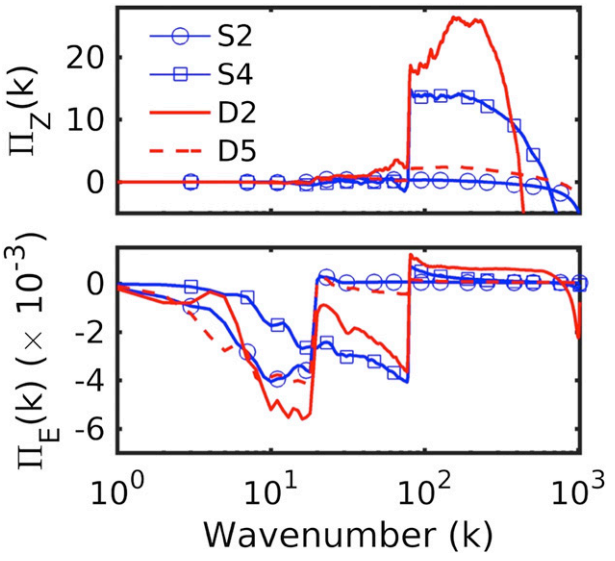

FIG. 6. (top) Enstrophy Π_Z and (bottom) Π_E kinetic energy transfer in Fourier space averaged over a sample calculated between simulation times 15 and 16 for every 500 time steps for runs S2, S4, D2, and D5.

the first energy source is dominant, and the spectral slope is closer to -3, consistent with synoptic-scale observations in the upper troposphere (Nastrom and Gage 1985). An important finding is that this transition takes place with a small amount of feedback from the mesoscale (e.g., $R_I = 8$ for D5 with -3 slope) compared to the magnitude of the primary (large scale) energy input, which can be attained by processes such as frontogenesis or atmospheric convective activity in the real atmosphere.

Figure 7a shows the results from the G series simulations (Table 4) along with D4 and D6 as reference to compare simulations with different separation scales between the energy inputs (the scale of the primary energy input is fixed). Note that the scale separation for G3, G4, and G5 is too large with the second energy source applied in the meso-β-scale range where vertical motions are significant in the atmosphere, and thus, these specific DNSs are not representative of realistic behavior, and they are used here for sensitivity purposes only. When the scale separation changes, the relative fraction of the energy input that turns to direct enstrophy flux (η_s/η_L) and inverse energy cascade ϵ_s/ϵ_L [Eqs. (4a) and (4b)] also changes. This change is very small for the cases of G1 and G2, but a higher amount of energy input is needed for the cases of G3 and G4 to support similar inverse energy flux rate as G1 and G2. This is illustrated in Fig. 7b, which shows the energy transfer $\Pi_E(k)$ for D4, G1, and G3. The results suggest that there is a preferred scale separation range to capture the scaling behavior of upper-tropospheric observations including the transition between -3 and $-5/3$ spectral slopes [shaded blue in Fig. 7a; see also Fig. 1 in Nastrom and Gage (1985)], which corresponds to the feedback between the meso-α and synoptic scales.

4. Conclusions

Previously, modeling studies of atmospheric turbulence have focused on either synoptic or mesoscale ranges, neglecting scale interactions between them. Here, it is demonstrated that a second energy injection is necessary to explain the -3 spectral slope between the synoptic scale and the mesoscale (see Fig. 1). The second energy input in the D series simulations is interpreted as a feedback mechanism from the meso-α scale to the synoptic scale, and the results suggest that even a small feedback is sufficient to support two-way transfers. Whereas assessing conclusively the implications of this feedback for the direction of net energy transfer under realistic atmospheric forcing is out of the scope of this work, these findings have important implications for explaining the observed energy spectra of atmosphere and to elucidate the impact of this mesoscale feedback on synoptic-scale predictability (Lorenz 1969; Berner et al. 2017), including the treatment of conservation laws across scales in weather and climate models (e.g., Thuburn 2008). The results presented here should be relevant to 2D geophysical turbulence with coexisting forward and inverse transfer such as the case of ocean circulation (e.g., Marino et al. 2015; McWilliams 2017), although the forcing and fluid properties and specific

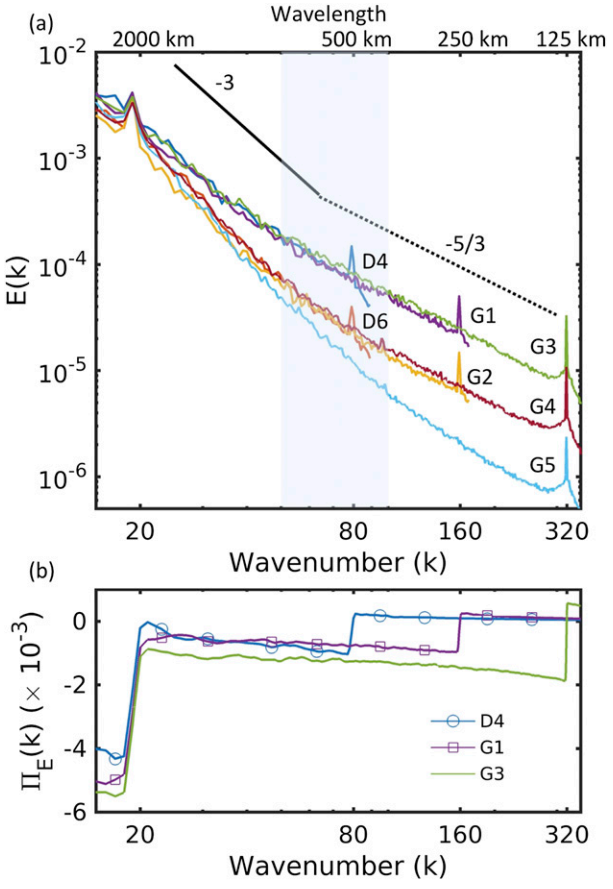

FIG. 7. (a) Energy spectra of D4, D6, and G series showing the spectra between the energy inputs for $T = 12.0$. The straight solid and dotted lines showing the −3 and −5/3 slope, respectively, are provided for reference. The shaded region marks the transition zone between about 800 and 400 km from the observations (Nastrom and Gage 1985). (b) The Π_E energy transfer in Fourier space for D4, G1, and G3 series.

range scales of interest may be different. Future studies of coupled 2D–3D interactions are necessary to elucidate energy transfer mechanisms and scale interactions at the mesoscale.

Acknowledgments. The simulations were made possible by the use of Mississippi State University High Performance Computing (HPC) facility. The authors thank three anonymous reviewers for insightful comments. The research was supported by the Pratt School of Engineering.

REFERENCES

Berner, J., and Coauthors, 2017: Stochastic parameterization: Toward a new view of weather and climate models. *Bull. Amer. Meteor. Soc.*, **98**, 565–588, https://doi.org/10.1175/BAMS-D-15-00268.1.

Bhushan, S., and Z. Warsi, 2007: Large eddy simulation of free-shear flows using an algebraic model. *Comput. Fluids*, **36**, 1384–1397, https://doi.org/10.1016/j.compfluid.2006.12.007.

Biferale, L., S. Musacchio, and F. Toschi, 2012: Inverse energy cascade in three-dimensional isotropic turbulence. *Phys. Rev. Lett.*, **108**, 164501, https://doi.org/10.1103/PhysRevLett.108.164501.

Boffetta, G., 2007: Energy and enstrophy fluxes in the double cascade of two-dimensional turbulence. *J. Fluid Mech.*, **589**, 253–260, https://doi.org/10.1017/S0022112007008014.

——, and S. Musacchio, 2010: Evidence for the double cascade scenario in two-dimensional turbulence. *Phys. Rev.*, **82E**, 016307, https://doi.org/10.1103/PhysRevE.82.016307.

——, and R. E. Ecke, 2012: Two-dimensional turbulence. *Annu. Rev. Fluid Mech.*, **44**, 427–451, https://doi.org/10.1146/annurev-fluid-120710-101240.

Borue, V., 1993: Spectral exponents of enstrophy cascade in stationary two-dimensional homogeneous turbulence. *Phys. Rev. Lett.*, **71**, 3967, https://doi.org/10.1103/PhysRevLett.71.3967.

Cencini, M., P. Muratore-Ginanneschi, and A. Vulpiani, 2011: Nonlinear superposition of direct and inverse cascades in two-dimensional turbulence forced at large and small scales. *Phys. Rev. Lett.*, **107**, 174502, https://doi.org/10.1103/PhysRevLett.107.174502.

Charney, J. G., 1971: Geostrophic turbulence. *J. Atmos. Sci.*, **28**, 1087–1095, https://doi.org/10.1175/1520-0469(1971)028<1087:GT>2.0.CO;2.

Cho, J. Y. N., and E. Lindborg, 2001: Horizontal velocity structure functions in the upper troposphere and lower stratosphere: 1. Observations. *J. Geophys. Res.*, **106**, 10 223–10 232, https://doi.org/10.1029/2000JD900814.

——, R. E. Newell, and J. D. Barrick, 1999: Horizontal wavenumber spectra of winds, temperature, and trace gases during the Pacific exploratory missions: 2. Gravity waves, quasi-two-dimensional turbulence, and vortical modes. *J. Geophys. Res.*, **104**, 16 297–16 308, https://doi.org/10.1029/1999JD900068.

Evans, K. J., P. H. Lauritzen, S. K. Mishra, R. B. Neale, M. A. Taylor, and J. J. Tribbia, 2013: AMIP simulation with the CAM4 spectral element dynamical core. *J. Climate*, **26**, 689–709, https://doi.org/10.1175/JCLI-D-11-00448.1.

Eyink, G. L., 1996: Exact results on stationary turbulence in 2D: Consequences of vorticity conservation. *Physica D*, **91**, 97–142, https://doi.org/10.1016/0167-2789(95)00250-2.

Frehlich, R., and R. Sharman, 2010: Climatology of velocity and temperature turbulence statistics determined from rawinsonde and ACARS/AMDAR data. *J. Appl. Meteor. Climatol.*, **49**, 1149–1169, https://doi.org/10.1175/2010JAMC2196.1.

Hamilton, K., Y. O. Takahashi, and W. Ohfuchi, 2008: Mesoscale spectrum of atmospheric motions investigated in a very fine resolution global general circulation model. *J. Geophys. Res.*, **113**, D18110, https://doi.org/10.1029/2008JD009785.

Kraichnan, R. H., 1967: Inertial ranges in two-dimensional turbulence. *Phys. Fluids*, **10**, 1417–1423, https://doi.org/10.1063/1.1762301.

——, 1971: Inertial-range transfer in two- and three-dimensional turbulence. *J. Fluid Mech.*, **47**, 525–535, https://doi.org/10.1017/S0022112071001216.

Lilly, D. K., 1989: Two-dimensional turbulence generated by energy sources at two scales. *J. Atmos. Sci.*, **46**, 2026–2030, https://doi.org/10.1175/1520-0469(1989)046<2026:TDTGBE>2.0.CO;2.

Lindborg, E., 2005: The effect of rotation on the mesoscale energy cascade in the free atmosphere. *Geophys. Res. Lett.*, **32**, L01809, https://doi.org/10.1029/2004GL021319.

——, 2006: The energy cascade in a strongly stratified fluid. *J. Fluid Mech.*, **550**, 207–242, https://doi.org/10.1017/S0022112005008128.

——, and K. Alvelius, 2000: The kinetic energy spectrum of the two-dimensional enstrophy turbulence cascade. *Phys. Fluids*, **12**, 945, https://doi.org/10.1063/1.870379.

Lorenz, E. N., 1969: Atmospheric predictability as revealed by naturally occurring analogues. *J. Atmos. Sci.*, **26**, 636–646, https://doi.org/10.1175/1520-0469(1969)26<636:APARBN>2.0.CO;2.

Marino, R., P. D. Mininni, D. Rosenberg, and A. Pouquet, 2013: Inverse cascades in rotating stratified turbulence: Fast growth of large scales. *Europhys. Lett.*, **102**, 44006, https://doi.org/10.1209/0295-5075/102/44006.

——, A. Pouquet, and D. Rosenberg, 2015: Resolving the paradox of oceanic large-scale balance and small-scale mixing. *Phys. Rev. Lett.*, **114**, 114504, https://doi.org/10.1103/PhysRevLett.114.114504.

McWilliams J. C., 2017: Submesoscale currents in the ocean. *Proc. Roy. Soc. London*, **472A**, 20160117, https://doi.org/10.1098/rspa.2016.0117.

Nastrom, G. D., and K. S. Gage, 1985: A climatology of atmospheric wavenumber spectra of wind and temperature observed by commercial aircraft. *J. Atmos. Sci.*, **42**, 950–960, https://doi.org/10.1175/1520-0469(1985)042<0950:ACOAWS>2.0.CO;2.

Nogueira, M., and A. P. Barros, 2014: The nonconvective/convective structural transition in stochastic scaling of atmospheric fields. *J. Geophys. Res. Atmos.*, **119**, 13 771–13 794, https://doi.org/10.1002/2014JD022548.

Pope, S. B., 2000: *Turbulent Flows.* Cambridge University Press, 771 pp.

Skamarock, W. C., 2004: Evaluating mesoscale NWP models using kinetic energy spectra. *Mon. Wea. Rev.*, **132**, 3019–3032, https://doi.org/10.1175/MWR2830.1.

——, S. H. Park, J. B. Klemp, and C. Snyder, 2014: Atmospheric kinetic energy spectra from global high-resolution nonhydrostatic simulations. *J. Atmos. Sci.*, **71**, 4369–4381, https://doi.org/10.1175/JAS-D-14-0114.1.

Sun, Y. Q., R. Rottuno, and F. Zhang, 2017: Contributions of moist convection and internal gravity waves to building the atmospheric −5/3 kinetic energy spectra. *J. Atmos. Sci.*, **74**, 185–201, https://doi.org/10.1175/JAS-D-16-0097.1.

Thuburn, J., 2008: Some conservation issues for the dynamical cores of NWP and climate models. *J. Comput. Phys.*, **227**, 3715–3730, https://doi.org/10.1016/j.jcp.2006.08.016.

Tung, K. K., and W. W. Orlando, 2003a: The k^{-3} and $k^{-5/3}$ energy spectrum of atmospheric turbulence: Quasigeostrophic two-level model simulation. *J. Atmos. Sci.*, **60**, 824–835, https://doi.org/10.1175/1520-0469(2003)060<0824:TKAKES>2.0.CO;2.

——, and ——, 2003b: On the differences between 2D and QG turbulence. *Discrete Contin. Dyn. Syst.*, **3B**, 145–162, https://doi.org/10.3934/dcdsb.2003.3.145.

Vallgren, A., and E. Lindborg, 2011: The enstrophy cascade in forced two-dimensional turbulence. *J. Fluid Mech.*, **671**, 168–183, https://doi.org/10.1017/S0022112010005562.

——, E. Deusebio, and E. Lindborg, 2011: Possible explanation of the atmospheric kinetic and potential energy spectra. *Phys. Rev. Lett.*, **107**, 268501, https://doi.org/10.1103/PhysRevLett.107.268501.

Waite, M. L., and C. Snyder, 2009: The mesoscale kinetic energy spectrum of a baroclinic life cycle. *J. Atmos. Sci.*, **66**, 883–901, https://doi.org/10.1175/2008JAS2829.1.

Xia, H., D. Byrne, G. Falkovich, and M. Shats, 2011: Upscale energy transfer in thick turbulent fluid layers. *Nat. Phys.*, **7**, 321–324, https://doi.org/10.1038/nphys1910.